Online Resource 1

Article title: "Chemical zonation in olivine-hosted melt inclusions"

Contributions to Mineralogy and Petrology (2014)

Authors: M.E. Newcombe*, A. Fabbrizio, Youxue Zhang, C. Ma, M. Le Voyer, Y. Guan, J. Eiler, A. Saal, E.M. Stolper

**Division of Geological and Planetary Sciences, California Institute of Technology, Pasadena, CA 91125, USA (megan@gps.caltech.edu)*

Contents:

S1. Further description of the model

S1.1 Forward model of MgO evolution in melt inclusions in response to cooling and crystallization of olivine

In this section, we describe in detail the equations used to calculate the distribution of MgO in an olivine-hosted melt inclusion in response to a given thermal history.

Diffusion of MgO in an (assumed spherical) melt inclusion is described by the radial component of the diffusion equation in spherical polar coordinates:

$$\frac{\partial C}{\partial t} = D\left(\frac{\partial^2 C}{\partial r^2} + \frac{2}{r}\frac{\partial C}{\partial r}\right) \tag{S1}$$

In equation (S1), C is the concentration of MgO (in wt. %), t is time (in seconds), r is the radial distance measured from the center of the melt inclusion (in meters) and D is the diffusivity of MgO (in m^2s^{-1}). D is assumed to be temperature-dependent, but not concentration- or radius-dependent. The initial condition ($C(r,0) = C_0$) and the boundary conditions ($C(a,t) = C_b$ and $\partial C/\partial r|_{r=0} = 0$, where a is the radius of the melt inclusion and C_b may depend on time) are discussed in the main text (see "Using zonation in melt inclusions to derive thermal histories: Description of the forward model").

By making the substitution $w=Cr$, equation (S1) can be reduced to the one dimensional diffusion equation:

$$\frac{\partial w}{\partial t} = D\frac{\partial^2 w}{\partial r^2} \tag{S2}$$

Equation (S2) can be non-dimensionalized using the following transformations:

$$x = \frac{r}{a} \tag{S3}$$

$$u = \frac{rC}{aC_0} = \frac{xC}{C_0} \tag{S4}$$

$$dt' = \frac{Ddt}{a^2} \tag{S5}$$

Applying transformations (S3) and (S4), equation (S2) becomes

$$\frac{a^2}{D}\frac{\partial u}{\partial t} = \frac{\partial^2 u}{\partial x^2} \tag{S6}$$

Similarly, the initial condition transforms to

$$u(x,0) = x \tag{S7}$$

and the boundary condition at $r=a$ becomes

$$u(x=1,t') = \frac{C_b}{C_0} \tag{S8}$$

Equations (S6)–(S8) are discretized using a forward-time, centered-space (FTCS) explicit scheme:

$$u_i^{j+1} = u_i^j + \frac{\Delta t'}{(\Delta x)^2}\left(u_{i+1}^j + u_{i-1}^j - 2u_i^j\right) \tag{S9}$$

In equation (S9), we adopt the notation $u(i\Delta x, j\Delta t) = u_i^j$. Since D is temperature-dependent (and therefore time-dependent in the cooling rate calculations we have done), $\Delta t'$ is calculated using the geometric average of $D(t)$ and $D(t+\Delta t)$:

$$\Delta t' = \frac{\sqrt{D(t)\cdot D(t+\Delta t)}}{a^2}\Delta t \tag{S10}$$

Once $u(x,t')$ has been calculated, $C(r,t)$ is found via the following transformation:

$$C(r,t) = \frac{uC_0}{x} \tag{S11}$$

S1.2 Calculation of olivine growth rate

As described in the main text (see "Testing the two-stage linear cooling model – 2. Modeling zonation of Al_2O_3"), the amount of olivine crystallized on the walls of the melt inclusion is calculated at each time step using mass balance arguments: The amount of MgO extracted from the melt at each time step is converted into a corresponding volume of olivine of a constant composition. The volume of olivine crystallized is then divided by the surface area of the (assumed spherical) melt inclusion to estimate the distance propagated by the olivine crystallization front during the time step.

The amount of MgO (in wt. %) extracted from the melt at each time step (ΔM) is calculated as follows:

$$\Delta M = \int \Delta C \cdot \mathrm{d}\left(\frac{4\pi r^3}{3}\right) \tag{S12}$$

ΔM calculated in equation (S12) can be converted into olivine growth distance using the following expression:

$$L = \frac{\Delta M}{C_{olivine} - C_0}\cdot\frac{\rho_{melt}}{\rho_{olivine}}\cdot\frac{1}{4\pi a^2} \tag{S13}$$

The first term of equation (S13) converts the mass of MgO extracted from the melt into a mass of olivine produced ($C_{olivine}$ is the mass fraction of MgO (in wt. %) in olivine, which is assumed to be a constant; C_0 is the initial mass fraction of MgO (in wt. %) measured in the melt inclusion). The second term converts this mass of olivine produced into a volume, accounting for the difference between the density of the melt (ρ_{melt}) and the density of the olivine ($\rho_{olivine}$), both of which are assumed to be constant with values of 2700 kg m^{-3} and 3250 kg m^{-3} respectively. The final term of equation (S13) divides the volume of olivine produced by the surface area of the melt inclusion in order to determine the width of the olivine growth rim on the walls of the inclusion (L). Knowledge of the width of the olivine growth rim at each time step was then used to calculate the olivine growth rate (V):

$$V = \frac{\Delta L}{\Delta t} \tag{S14}$$

S2. Errors introduced by assumptions of the model

S2.1 Assumption that olivine-melt boundary is fixed: Recalculation of MgO profiles in the melt inclusions considering olivine growth

The model described in section S1.1 uses a boundary condition that is fixed at $r=a$ and does not consider the effects of olivine growth on the walls of the melt inclusion. Typical modeling results for the natural inclusions studied in the paper show a post-entrapment growth of about 1 μm thick olivine layer (meaning boundary motion of 1 μm) in a melt inclusion of about 100 μm radius. That is, the total effect of the boundary motion is not significant. In each time step, the boundary motion is of the order 0.001 μm. Accounting for the boundary motion would significantly increase the complexity of the programing. In this section we describe another method for calculating the distribution of MgO in the melt inclusions, this time considering the effects of olivine growth. The approach taken for this recalculation of MgO is similar to the calculation of Al_2O_3 evolution in the melt inclusions described in the main text (see "Testing the two-stage linear cooling model – 2. Modeling zonation of Al_2O_3").

As described in section S1.1, we wish to solve the radial component of the spherical diffusion equation (equation S1), with a homogenous concentration of MgO as the initial condition. We define the new boundary condition as follows:

$$D\left.\frac{\partial C}{\partial r}\right|_{r=a} = V\left(C_{r=a} - C_{olivine}\right) = -\left(K_d - 1\right)VC_{r=a} \tag{S15}$$

In equation (S15), $C_{r=a}$ is the concentration of MgO (in wt. %) in the melt at the olivine-melt interface, $C_{olivine}$ is the concentration of MgO (in wt. %) in the olivine, and K_d is the olivine-melt partition coefficient ($K_d = C_{olivine} / C_{r=a}$). K_d is known to be dependent on melt composition and temperature (e.g., Roeder and Emslie 1970) and likely changes from ~4 to ~9 during cooling and crystallization of the melt inclusions. However, for simplicity, we assume a constant value of $K_d = 6$ throughout the simulation.

The boundary condition in equation (S15) can be non-dimensionalized following transformations (S3)–(S4) and introducing the dimensionless variable b, defined as $b = aV / D$:

$$\left.\frac{\partial u}{\partial x}\right|_{x=1} = \left(1 - b\left[K_d - 1\right]\right)u_{x=1} \tag{S16}$$

The numerical scheme is the same as described in section S1.1, apart from the boundary condition at $x = 1$, which becomes:

$$u_{N,j} = \frac{u_{N-1,j}}{1 - \left(1 - b\left[K_d - 1\right]\right)\Delta x} \tag{S17}$$

In equation (S17), $u_{N,j}$ represents the dimensionless concentration of MgO in the melt at the olivine-melt interface.

The results of the recalculation of MgO with boundary condition (S16) are shown in Figure S1 for melt inclusion Siq16. The two methods of calculating MgO are in good agreement. The slight differences between the two calculations that are visible near the inclusion edge are probably primarily due to the inaccuracy of the assumption that K_d has a constant value of 6.

S2.2 Use of Chen and Zhang (2008) thermometer

The largest source of error in our calculation of cooling histories is the choice of relationship between temperature and MgO concentration in the melt at the olivine-melt interface. There are many published parameterizations of the temperature dependence of the MgO concentration of melt in equilibrium with olivine (e.g., Roeder and Emslie 1970; Sugawara 2000; Chen and Zhang 2008; Putirka 2008; Matzen et al. 2011) and also many published olivine-liquid equilibrium models (Ford et al. 1983; Beattie 1993; Ghiorso and Sack 1995). We opted for the relatively simple model of Chen and Zhang (2008), which, in addition to simplicity, also has the advantage that the experiments used to determine the temperature dependence of MgO concentration in the liquid at the olivine-melt interface were also used to determine the temperature dependence of the diffusivity of MgO in the melt (which is another important parameter in our model). However, the MgO-temperature parameterization of Chen and Zhang (2008) was determined by fitting the results of olivine dissolution experiments (dissolution of San Carlos olivine with a composition of $Fo_{90.6}$ into a basaltic melt), and so an implied assumption of this model is that the olivine has a constant composition of $Fo_{90.6}$. In reality, the composition of the host olivine of the Siqueiros melt inclusions decreases from ~Fo_{90} far (i.e., $\gtrsim$20 μm) from the inclusions to ~Fo_{88} at the olivine-melt interface (as measured by electron microprobe – see Online Resource 2), and the composition of the olivine adjacent to the Galapagos inclusions can be as low as Fo_{82}. If higher resolution analytical techniques were available, it is possible that an even stronger decrease in the forsterite content of the olivine could be observed right at the olivine-melt interface. This assumption in the modeling that the temperature reflects MgO partitioning between the melt and San Carlos olivine is thus an imperfect approximation and results in an underestimation of the temperature of equilibration of the olivine and melt at the outer edges of the melt inclusions (~50°C for the Siqueiros inclusions and up to ~70°C for the Galapagos inclusions).

To assess the potential error in our best-fit cooling rates introduced by using the Chen and Zhang (2008) parameterization rather than a more complex olivine-liquid equilibrium model, we ran a MELTS fractional crystallization calculation on the composition measured in the centre of inclusion Siq16, and we used the results of this calculation to predict the MgO concentration in the melt as olivine crystallization progressed. We found that, for a given MgO concentration in equilibrium with olivine, MELTS predicts temperatures that are ~50 °C higher than temperatures predicted by the Chen and Zhang (2008) parameterization. We fit inclusion Siq16 using the MgO-temperature relationship found by MELTS, and compare the results to fitting with the Chen and Zhang MgO-temperature relationship in Figures S2 and S3. We find that the best-fit cooling rates found using the MELTS MgO-temperature relationship are approximately a factor of two higher than the best-fit cooling rates found using the Chen and Zhang (2008) MgO-temperature parameterization (Figure S3). The quality of the fit to the MgO data in melt inclusion Siq16 is the same for both MgO-temperature relationships. Although the choice of MgO-temperature parameterization is a source of uncertainty for our cooling rate model, it does not alter the conclusions of the study.

S2.3 Error in the calculated amount of olivine growth

The assumption of a constant olivine composition of $Fo_{90.6}$ affects not only the estimated temperature of olivine-melt equilibrium, but also affects the calculated mass of olivine growth during cooling and crystallization. As described in section S1.2, the amount of olivine growth is calculated by mass balance of MgO loss from the melt inclusions. The composition of the growing olivine is an important parameter in this calculation; the more forsteritic the olivine is assumed to be, the less olivine can grow from a given mass of MgO. Since we have slightly overestimated the forsterite content of the growing olivine, we must also have underestimated the mass of olivine growth. Although the olivine growth rate does not affect the derived cooling histories, it does affect the calculated distribution of Al_2O_3 in the melt inclusions. We have used MELTS calculations (described in the previous section) to explore the likely magnitude of this effect for inclusion Siq16. The results are presented in Figures S4 and S5.

S2.4 Choice of T_{high}

As explained in the main text (see "Using zonation in melt inclusions to derive thermal histories"), two-stage linear cooling histories are defined by five parameters: A starting temperature (T_{high}), an intermediate temperature at which the cooling rate changes (T_{mid}), a final temperature (T_{low}), and two cooling rates (q_1 and q_2). In our model, we treat T_{mid}, q_1, and q_2 as free parameters, and T_{high} and T_{low} are calculated from measured MgO concentrations using equation (1). T_{low} is calculated using the lowest measured MgO concentration at the edge of each melt inclusion. Similarly, T_{high} is calculated using the initial concentration of MgO in each melt inclusion (see equation (1)). However, the initial concentration of MgO in the melt inclusions could be chosen in a number of ways, and this results in some uncertainty in the estimation of T_{high}. We considered four choices of initial MgO concentration:

i. **Initial MgO concentration calculated to be in equilibrium with the far-field olivine host:** This choice of initial condition results in high values of T_{high} (up to 1252 °C). The lack of MgO data between this choice of initial concentration of MgO (up to 12.8 wt. % MgO) and the highest measured concentration of MgO in the melt inclusions (up to 9.5 wt. % MgO) results in the inversion problem being very poorly constrained. The misfit between the model and the data is greater when this initial condition is applied than the misfit obtained using the initial conditions described below.

ii. **Initial MgO concentration chosen to match the composition of the matrix glass:** This choice of initial condition also results in high values of T_{high} for the Siqueiros melt inclusions, and therefore a poorly constrained inversion problem. The Galapagos matrix glasses are more evolved than their associated melt inclusions, so this choice of initial condition would not be appropriate for the Galapagos melt inclusions.

iii. **Initial MgO concentration chosen as the highest measured MgO concentration in each individual melt inclusion:** This choice of initial condition results in lower values of T_{high} (up to 1171 °C) compared to method **i**. The inversion problem is well constrained with this choice of initial MgO concentration. However, choosing a different starting MgO concentration for each melt inclusion based on its highest measured MgO concentration results in the introduction of a bias in the fitting procedure, because small melt inclusions tend to have lower central concentrations of MgO than large inclusions (see Figure 5 in the main text).

iv. **Initial MgO concentration chosen as the highest MgO concentration measured among all melt inclusions from the same sample locality:** This is our preferred method of estimating the initial concentration of MgO in the melt inclusions and is explained in detail in the main text (see "Using zonation in melt inclusions to derive thermal histories: Description of the forward model").

S2.5 Choice of T_{low}

For the fitting procedure presented in the main text, the lowest temperature considered by the model (T_{low}) is the temperature corresponding to the lowest MgO concentration measured at the edges of each melt inclusion (except where pairs of inclusions were fit together, in which case, the lowest measured MgO in the pair of inclusions was used to calculate T_{low}). This temperature is typically ~1000 °C for the Siqueiros melt inclusions. An alternative way to set this temperature would be to allow the model to run all the way down to a temperature comfortably past the closure temperature for MgO diffusion (MgO diffusion becomes negligible in this system at ~700 °C over a timescale of 1 hour), or even to seawater temperature (~2 °C). We tried these methods of setting T_{low}, and found that it made little difference to the shapes of the

model MgO curves (Figures S6 and S7). However, the misfit between the model and the MgO data in the melt inclusions was reduced when we set T_{low} to the temperature corresponding to the lowest MgO concentration measured at the edges of each melt inclusion, so we chose to adopt this approach for the fitting presented in the main paper. We have tested the effect on the best-fit cooling rates for melt inclusion Siq16 determined by fixing T_{low} to 600 °C, and find that this assumption increases the best-fit value of q_1 by a factor of ~2, and increases the best-fit value of q_2 by a factor of ~3 (Figure S8).

It should be noted that our MgO concentration profiles provide little constraint as to how the melt inclusions cool from ~1000 °C to seawater temperature, and constraint of the cooling history over this temperature range would require much higher spatial resolution data at the edges of the melt inclusions than we are currently able to achieve with the electron microprobe. It is also possible that the assumption of equilibrium between the crystallizing olivine and the adjacent melt at these low temperatures may break down, such that the boundary condition assumed by our model is no longer applicable.

S2.6 Assumption that melt inclusions are cut through their centers

When preparing melt inclusions for this study, care was taken to expose the maximum possible surface area of the melt inclusions during polishing, such that the exposed sections of the melt inclusions passed approximately through their centers. However, for olivine crystals hosting multiple inclusions, it is difficult to cut every melt inclusion through its center, and it is likely that some of the inclusions were under- or over-exposed.

We explore the effect of an off-center cut through a melt inclusion on the resultant profiles of MgO and Al_2O_3 in Figure S9. When a chemically zoned melt inclusion is cut along a plane that is far from the center of the inclusion, it samples more of the diffusive boundary layer. Concentration profiles across such a plane will be relatively depleted in MgO and enriched in Al_2O_3. In the main text (see "Testing the two-stage linear cooling model – 2. Modeling zonation of Al_2O_3"), we calculate the distribution of Al_2O_3 across a pair of melt inclusions hosted in the same olivine crystal, and we find that the smaller inclusion of the pair requires a higher starting concentration of Al_2O_3 than the larger inclusion in order to match the data. Although it is likely in this case that the inclusions trapped different melt compositions (given the differences in Sr/Sr* between the inclusions, and the variability of Al_2O_3 in the Siqueiros inclusions more generally), it is also possible that an off-center cut through the smaller inclusion contributed to its elevated Al_2O_3 concentration.

S3. Inversion tests

We designed a number of inversion tests to answer the following questions:

- When given data from a melt inclusion with a known two-stage linear cooling history, does our inversion technique find the correct cooling history parameters?
- What is the effect of melt inclusion size on the ability of the inversion technique to find the correct cooling history parameters?
- What is the effect of changing the spatial resolution (i.e., the point spacing) of concentration measurements?
- What is the effect of overestimating the starting temperature?

We created synthetic MgO concentration data for melt inclusions with radii of 50 and 150 μm, by running the forward model described in the main text (see "Description of the forward model") with T_{high}=1440 K, T_{mid}=1400 K, T_{low}=1300 K, q_1=600 K hr^{-1}, and q_2=6000 K hr^{-1}. The synthetic profiles were sampled at 2 and 10 μm point spacing.

We inverted the synthetic profiles using the technique described in the main text (see "Inverting the MgO concentration profiles for two-stage linear cooling histories"). Noise was added to the synthetic data to create 100 "noisy" MgO concentration profiles, by assuming normally distributed data with 1σ=0.1 wt. %

MgO. A best-fit two-stage linear cooling history was found for each of these noisy profiles. The cooling history parameters for the synthetic data were determined by calculating the median values of q_1, q_2, and T_{mid} found by the parametric bootstrap fitting procedure described in the main text. This process is illustrated in Figure S10 for a synthetic melt inclusion with a radius of 150 μm and a point spacing of 10 μm.

S3.1 Testing the accuracy of the inversion technique

In Figure S11, we present the results of inverting the MgO concentration profile across a model melt inclusion with a radius of 150 μm and a point spacing of 10 μm. The inversion technique returns cooling history parameters that are within 4% of their true values (parameter values returned by inversion: q_1=578.2 K/hr, q_2=6064 K/hr, T_{mid}=1400.3 K; true parameter values: q_1=600 K/hr, q_2=6000 K/hr, T_{mid}=1400 K). The best-fit values of q_1 and q_2 are not normally distributed, and tend to be skewed towards higher cooling rates, particularly for small melt inclusions with fewer data points; this is because, beyond a certain point, increasing the cooling rate to higher values has little effect on the resultant distribution of MgO within the melt inclusions. Due to this asymmetry in the distribution of best-fit parameters, we find that the median of the best-fit parameters is a better proxy for the true parameter values than the mean.

S3.1.1 Effect of melt inclusion size

We have tested the effect of melt inclusion size on the accuracy and precision of the inversion technique. The results are presented in Figure S12 for two model melt inclusions with different radii (50 and 150 μm) that both underwent the same thermal history (T_{high}=1440 K, T_{mid}=1400 K, T_{low}=1300 K, q_1=600 K hr^{-1}, and q_2=6000 K hr^{-1}). MgO concentrations across both melt inclusions were sampled at 10 μm intervals, such that the 150 μm inclusion contained three times as many data points as the 50 μm inclusion. The accuracy of the inversion technique was not greatly affected for the small inclusion: values of q_1, q_2 and T_{mid} determined by the inversion technique were within 6% of their true values. However, the precision of the inversion technique was lower for the 50 μm inclusion (precision can be assessed by the spread of best fits to noisy profiles in Figure S12, and the sizes of the 95% confidence ellipses).

S3.1.2 Effect of spatial resolution of MgO measurements

In this section, we explore the effect of the spacing of MgO concentration measurements in a melt inclusion on the accuracy and precision of our cooling history inversion technique. As explained in the main text (see the "Analytical techniques" section), in the early phases of the study, the electron microprobe beam diameter was set to 5 μm with a point spacing of 10 μm. In order to improve spatial resolution, later profiles were measured with a focused beam (with a nominal diameter of ~150 nm) and a point spacing of 1–2 μm.

To test for the effect of spatial resolution on our inversion technique, we ran a forward model for a melt inclusion with a radius of 150 μm with the following cooling history parameters: T_{high}=1440 K, T_{mid}=1400 K, T_{low}=1300 K, q_1=600 K hr^{-1}, and q_2=6000 K hr^{-1}. The resultant MgO concentration profile was sampled with a 2 μm point spacing ('high spatial resolution') and a 10 μm point spacing ('low spatial resolution'). Cooling histories were fit to both the high spatial resolution and the low spatial resolution profiles using our inversion technique, and the results are presented in Figure S13. The reduction of the point spacing from 10 to 2 μm leads to a significant reduction in the size of the 95% confidence ellipse around the best-fit cooling history parameters. For this reason, in the main text, we focus on the melt inclusions whose MgO concentrations were measured with high spatial resolution.

S3.1.3 Effect of overestimating T_{high}

As discussed above, we have used our forward model to create MgO data for a synthetic melt inclusion with a radius of 150 μm with the following cooling history parameters: T_{high}=1440 K, T_{mid}=1400 K, T_{low}=1300 K, q_1=600 K hr^{-1}, and q_2=6000 K hr^{-1}. We have assessed the effects on our inversion technique of overestimating T_{high} by inverting this synthetic MgO data assuming T_{high}=1480 K (instead of the true value of T_{high}=1440 K). The results of this inversion are shown in Figure S14. When T_{high} is overestimated, q_1 and q_2 are forced to take lower values. The value of q_1 must be low to allow sufficient

diffusive relaxation of MgO to reproduce the flat MgO concentration profile across the center of this melt inclusion. The curvature at the edges of the profile must then be produced solely during the second stage of cooling. This forces q_2 to take a value that compromises between the high value required to reproduce the steep gradient near the olivine-melt interface and the lower value required to reproduce the shallowing of this gradient from edge to center.

S4. Comparison of the 1-stage and 2-stage models

Figure S15 compares the best-fit cooling rates from the second stage of the two-stage linear cooling model (q_2) with the cooling rates fit to the single-stage cooling model (q). Overall, the single-stage cooling rate correlates with the cooling rate during the second stage of cooling (q_2) in the two-stage model. For some inclusions (Siq7, Gal-AHA2-27, Gal-STG17, and Gal-STG-48; labeled in red on Figure S15), the two rates agree within error (where the error bars represent two standard deviations), but for others (Gal-AHA2-24, Siq8, Siq13, Siq15, and Siq16; labeled in black on Figure S15), q_2 is higher than q by up to a factor of ~2. The latter inclusions are the ones for which the shallow central gradient in MgO concentration is most pronounced (Figure 9 of main paper), so they are less well described by the single-stage cooling model (i.e., the fits are poorer, see Figure S15b). In these cases, the single-stage cooling model has been forced to compromise between the low cooling rate required to fit the shallow MgO gradient in the center of the inclusions and the fast rate required to fit the sharp MgO gradient at the edges of the inclusions, explaining why the single stage rate is lower than q_2 (Figure S15c). For the inclusions that are well fit by the single-stage model, q and q_2 are similar (Figure S15c; labeled in red), as are the misfits of the two models (Figure S15b; labeled in red).

There is a bias in our fitting procedure for the single-stage cooling model that results in large melt inclusions being fit by lower cooling rates than small inclusions (Figure S15a). This effect can be understood in the context of the best-fit multi-stage cooling histories, which always have an initial period of slow cooling and a final stage of rapid cooling: In small inclusions, diffusion of MgO from the boundary layer produced during the final period of rapid cooling may reach the center of the inclusion and thereby erase nearly all evidence for the prior period of slow cooling. In large inclusions, however, the shallow central gradient of MgO produced during slow cooling can be preserved during the final stage of rapid cooling, because there may not be enough time for the MgO boundary layer produced at the edges of the melt inclusion during rapid cooling to propagate into the center of the inclusion. This would produce the correlation between single-stage cooling rates and inclusion size observed in Figure S15a for those inclusions not well fit by a single-stage cooling history (labeled in black). Note that this correlation does not exist for those inclusions that are well fit by the single-stage cooling model (labeled in red on Figure S15a), including the two subaerially erupted melt inclusions (Gal-STG-17 and Gal-STG-48), suggesting that the high cooling rates recorded by these two inclusions are not simply an artifact of their small size.

S5. Comparison of cooling rates determined by our model with cooling rates expected for conductive cooling

The results of a simple conductive cooling model are shown in Figure S16. For these calculations, the diffusivity of heat was assumed to be 1×10^{-6} m^2s^{-1}, and we used an analytical expression for diffusion in a semi-infinite medium (Crank 1975). The temperature at the interface between the lava and the seawater was held at a constant value of 2 °C, and the initial temperature of the lava was set to 1200 °C.

The results of this simple calculation show that the range of cooling rates determined for the Siqueiros melt inclusions by our technique (~300 – 10,000 °C/hr) is consistent with conductive cooling of the melt

inclusions at distances of a few centimeters from the lava-water interface. The Siqueiros melt inclusions were sampled from pillow-rim glass, which typically extends no more than 1 – 2 cm from the lava-water interface, so the slightly greater distances from the lava-water interface implied by the conductive cooling model may reflect cooling during transport of the host olivine crystal from the interior to the edge of the pillow.

Cooling rates determined from fitting MgO concentration profiles in melt inclusions from a hornito on Santiago Island reach higher values (up to ~22,000 °C/hr) than those determined for the Siquieros melt inclusions. These higher values may reflect the small size of the pyroclasts (i.e., short distances from the melt inclusion to the lava-air interface) during this kind of eruption. The maximum cooling rates recorded by the Santiago inclusions are consistent with the passage of a conductive cooling front during cooling at a distance of 1 – 2 cm from the air-lava interface (Figure S16).

Table S1 Description of samples

Inclusion name	Sample ID	Saal et al. (2002)	Locality	References [b]	EMP point
Siq7	A25-D20-1	n/a	Siqueiros Fracture Zone	1, 2	2
Siq8	A25-D20-1	n/a	Siqueiros Fracture Zone	1, 2	2 and 10
Siq1-11a	2384-2	n/a	Siqueiros Fracture Zone	1, 2	10
Siq1-11b	2384-2	2-8-1	Siqueiros Fracture Zone	1, 2	10
Siq1-12a	2384-2	n/a	Siqueiros Fracture Zone	1, 2	10
Siq1-12b	2384-2	2-7-2	Siqueiros Fracture Zone	1, 2	10
Siq1-12c	2384-2	n/a	Siqueiros Fracture Zone	1, 2	10
Siq13	2384-9	n/a	Siqueiros Fracture Zone	1, 2	2
Siq15	2384-9	n/a	Siqueiros Fracture Zone	1, 2	2
Siq16	2384-9	n/a	Siqueiros Fracture Zone	1, 2	2
Siq1-19a	2384-2	2-3-1	Siqueiros Fracture Zone	1, 2	10
Siq1-19b	2384-2	2-3-2	Siqueiros Fracture Zone	1, 2	10
Siq1-24a	2384-3	n/a	Siqueiros Fracture Zone	1, 2	10
Siq1-24b	2384-3	3-10-2	Siqueiros Fracture Zone	1, 2	10
Siq1-24c	2384-3	3-10-1	Siqueiros Fracture Zone	1, 2	10
Siq2-47a	A25-D20-5	A-8-2	Siqueiros Fracture Zone	1, 2	10
Siq2-47b	A25-D20-5	A-8-1	Siqueiros Fracture Zone	1, 2	10
Siq2-52a	2384-9	9-1-2-2	Siqueiros Fracture Zone	1, 2	10
Siq2-52b	2384-9	9-1-2-1	Siqueiros Fracture Zone	1, 2	10
Siq2-53a	2384-9	9-1-1	Siqueiros Fracture Zone	1, 2	10
Siq2-53b	2384-9	n/a	Siqueiros Fracture Zone	1, 2	10
Siq3-56a	2384-6	n/a	Siqueiros Fracture Zone	1, 2	10
Siq3-56b	2384-6	6-3	Siqueiros Fracture Zone	1, 2	10
Siq3-65a	A25-D20-1	D-6-2	Siqueiros Fracture Zone	1, 2	10
Siq3-65b	A25-D20-1	D-6-3	Siqueiros Fracture Zone	1, 2	10
Siq3-65c	A25-D20-1	D-6-1	Siqueiros Fracture Zone	1, 2	10
Gal-AHA2-24	AHA D25C	n/a	Fernandina, Galapagos	3	2
Gal-AHA2-27	AHA D25C	n/a	Fernandina, Galapagos	3	2
Gal-STG13	STG06-29-13	n/a	Santiago, Galapagos	3	2
Gal-STG16b	STG06-29-16b	n/a	Santiago, Galapagos	3	2
Gal-STG16c	STG06-29-16c	n/a	Santiago, Galapagos	3	2
Gal-STG17	STG06-29-17	n/a	Santiago, Galapagos	3	2
Gal-STG20	STG06-29-20	n/a	Santiago, Galapagos	3	2
Gal-STG23	STG06-29-23	n/a	Santiago, Galapagos	3	2
Gal-STG48	STG06-29-48	n/a	Santiago, Galapagos	3	2

[a] Inclusion ID corresponds to names given to specific inclusions previously studied in Saal et al. (2002)

[b] References: 1. Saal et al. (2002) 2. Perfit et al. (1996) 3. Koleszar et al. (2009)

Table S2 Fitting results for the single-stage and two-stage cooling models, for all melt inclusions whose MgO concentration profiles have >5 points.

			Single-stage cooling model		Two-stage cooling model		
Inclusion name	T_{high} **(K)**	T_{low} **(K)**	q **(K/hr)**	**1σ (K/hr)**	q_1 **(K/hr)**	q_2 **(K/hr)**	T_{mid} **(K)**
Siq7	1413	1245	907	10.1	271	1195	1358
Siq8	1413	1264	1551	28.5	1113	2983	1324
Siq1-11b	1423	1318	401	14.3	174	1617	1369
Siq1-12b	1423	1268	560	15.4	265	4101	1319
Siq13	1444	1299	3197	76.2	815	7176	1399
Siq15	1444	1302	4239	99.8	1117	10313	1398
Siq16	1444	1280	3353	90.0	292	6305	1412
Siq1-19a	1423	1293	835	42.3	381	19937	1343
Siq1-19b	1423	1316	485	15.3	180	1694	1370
Siq1-24b	1441	1294	808	17.3	501	1497	1364
Siq1-24c	1441	1323	1311	72.3	389	3969	1389
Siq2-47a	1365	1246	662	31.0	507	8423	1267
Siq2-47b	1365	1254	708	37.0	1057	597	1305
Siq2-52a	1444	1355	1311	84.1	124	1603	1431
Siq2-52b	1444	1301	712	22.2	687	754	1327
Siq2-53a	1444	1354	523	26.7	14	723	1433
Siq3-56a	1417	1279	2864	141.7	552	3718	1361
Siq3-56b	1417	1313	2102	112.7	828	2144	1417
Siq3-65a	1413	1301	1119	29.8	693	1297	1372
Siq3-65b	1413	1320	1308	50.5	898	7407	1341
Gal-AHA2-24	1334	1151	155	3.4	64	323	1274
Gal-AHA2-27	1334	1289	4358	764.3	684	4689	1332
Gal-STG13	1402	1353	12720	1753	356	20243	1394
Gal-STG16b	1402	1317	4880	168	724	8342	1379
Gal-STG16c	1402	1303	6144	223	666	7123	1390
Gal-STG17	1402	1312	5889	395.9	140	7146	1394
Gal-STG20	1402	1334	12202	912	494	13473	1398
Gal-STG23	1402	1348	12086	1729	65	22207	1395
Gal-STG48	1402	1303	4360	182.2	609	8106	1379

S6. Additional references

Beattie P (1993) Olivine-melt and orthopyroxene-melt equilibria. Contributions to Mineralogy and Petrology 115 (1):103-111. doi:10.1007/bf00712982

Chen Y, Zhang Y (2008) Olivine dissolution in basaltic melt. Geochimica et Cosmochimica Acta 72 (19):4756-4777. doi:10.1016/j.gca.2008.07.014

Crank J (1975) The Mathematics of Diffusion. 2nd edn. Oxford University Press,

Ford C, Russell D, Craven J, Fisk M (1983) Olivine-liquid equilibria: temperature, pressure and composition dependence of the crystal/liquid cation partition coefficients for Mg, Fe2+, Ca and Mn. Journal of Petrology 24 (3):256-266

Ghiorso MS, Sack RO (1995) Chemical mass transfer in magmatic processes IV. A revised and internally consistent thermodynamic model for the interpolation and extrapolation of liquid-solid equilibria in magmatic systems at elevated temperatures and pressures. Contributions to Mineralogy and Petrology 119 (2):197-212

Koleszar AM, Saal AE, Hauri EH, Nagle AN, Liang Y, Kurz MD (2009) The volatile contents of the Galapagos plume; evidence for H_2O and F open system behavior in melt inclusions. Earth and Planetary Science Letters 287 (3–4):442-452. doi:10.1016/j.epsl.2009.08.029

Matzen AK, Baker MB, Beckett JR, Stolper EM (2011) Fe–Mg partitioning between olivine and high-magnesian melts and the nature of Hawaiian parental liquids. Journal of Petrology 52 (7-8):1243-1263

Perfit MR, Fornari DJ, Ridley WI, Kirk PD, Casey J, Kastens KA, Reynolds JR, Edwards M, Desonie D, Shuster R, Paradis S (1996) Recent volcanism in the Siqueiros transform fault: picritic basalts and implications for MORB magma genesis. Earth and Planetary Science Letters 141 (1–4):91-108. doi:10.1016/0012-821x(96)00052-0

Putirka KD (2008) Thermometers and barometers for volcanic systems. Reviews in Mineralogy and Geochemistry 69 (1):61-120

Roeder P, Emslie R (1970) Olivine-liquid equilibrium. Contributions to Mineralogy and Petrology 29 (4):275-289

Saal AE, Hauri EH, Langmuir CH, Perfit MR (2002) Vapour undersaturation in primitive mid-ocean-ridge basalt and the volatile content of Earth's upper mantle. Nature 419 (6906):451-455. doi:http://www.nature.com/nature/journal/v419/n6906/suppinfo/nature01073_S1.html

Sugawara T (2000) Empirical relationships between temperature, pressure, and MgO content in olivine and pyroxene saturated liquid. Journal of Geophysical Research 105 (B4):8457-8472

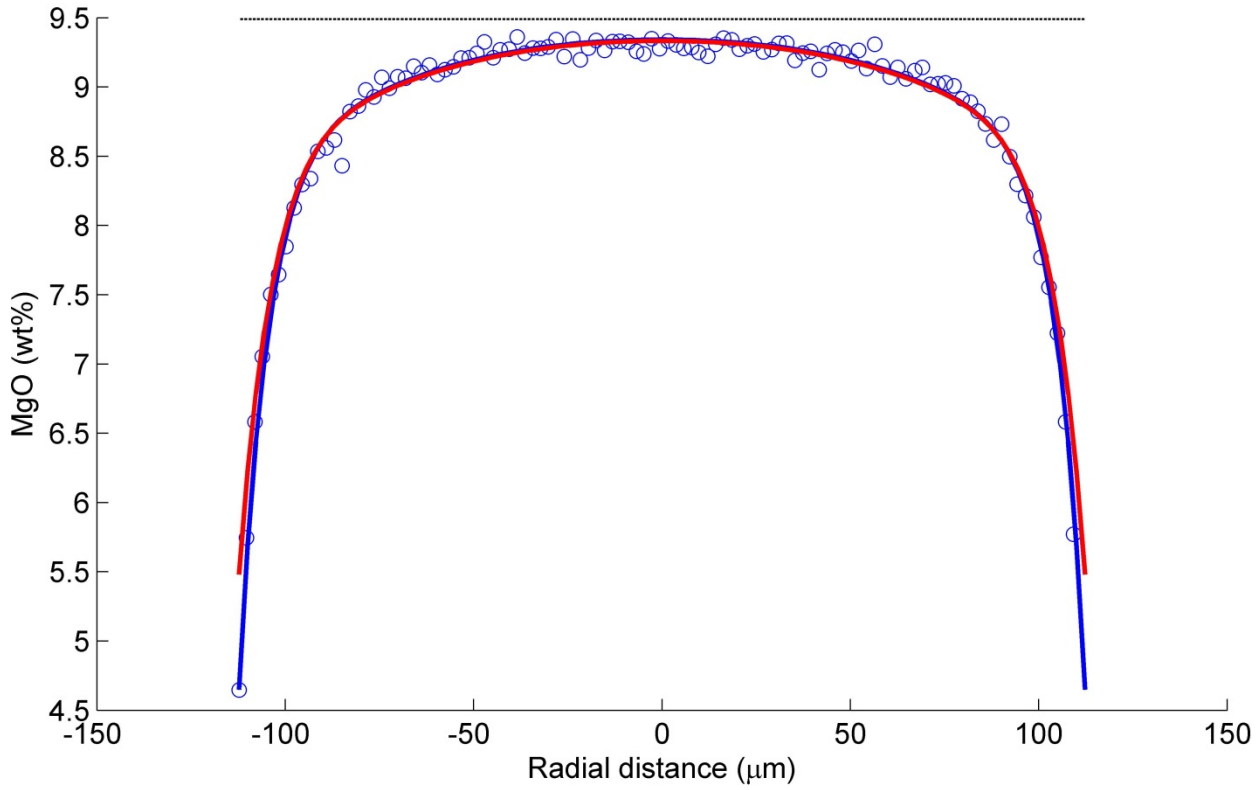

Figure S1 Comparison between two methods of calculating MgO distribution in melt inclusion Siq16. The initial concentration of MgO is assumed to be 9.5 wt. %). The best-fit two-stage linear cooling model (described in section S1.1 and the main text) is plotted in blue. The recalculation of MgO considering olivine growth (see section S1.3) is plotted in red.

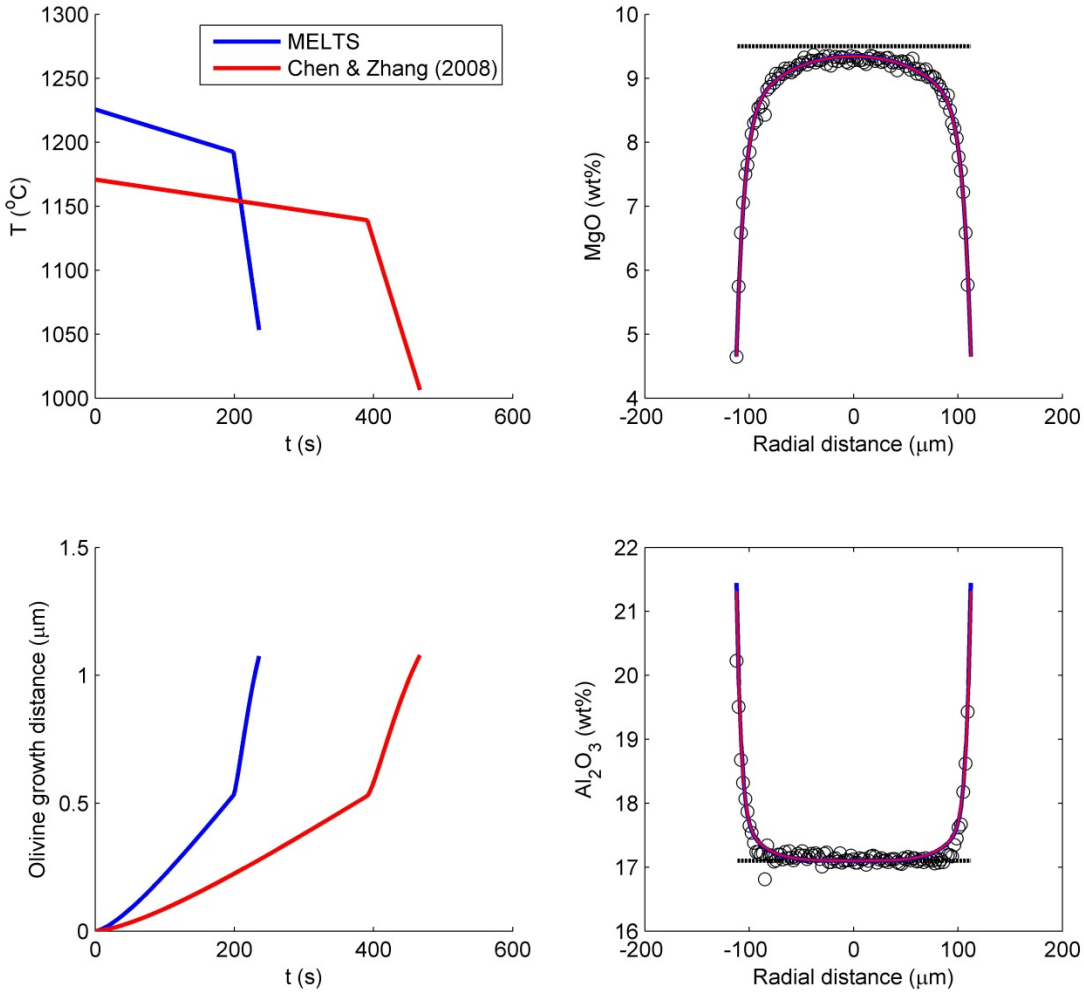

Figure S2 Comparison of best fits to MgO data from melt inclusion Siq16 using the MgO-temperature relationship of Chen and Zhang (2008) (in red) and MELTS (in blue). The MELTS calculation used the central composition of Siq16 as a starting composition and an oxygen fugacity of two log units below the NNO buffer (Saal et al. 2002). The fits to the data were equally good for both models. The MELTS thermometer predicts a higher temperature for a given MgO concentration in the liquid than the Chen and Zhang (2008) thermometer (see discussion in S2.2), and this results in higher cooling rates and a shorter duration of cooling by approximately a factor of two when the MELTS thermometer is used.

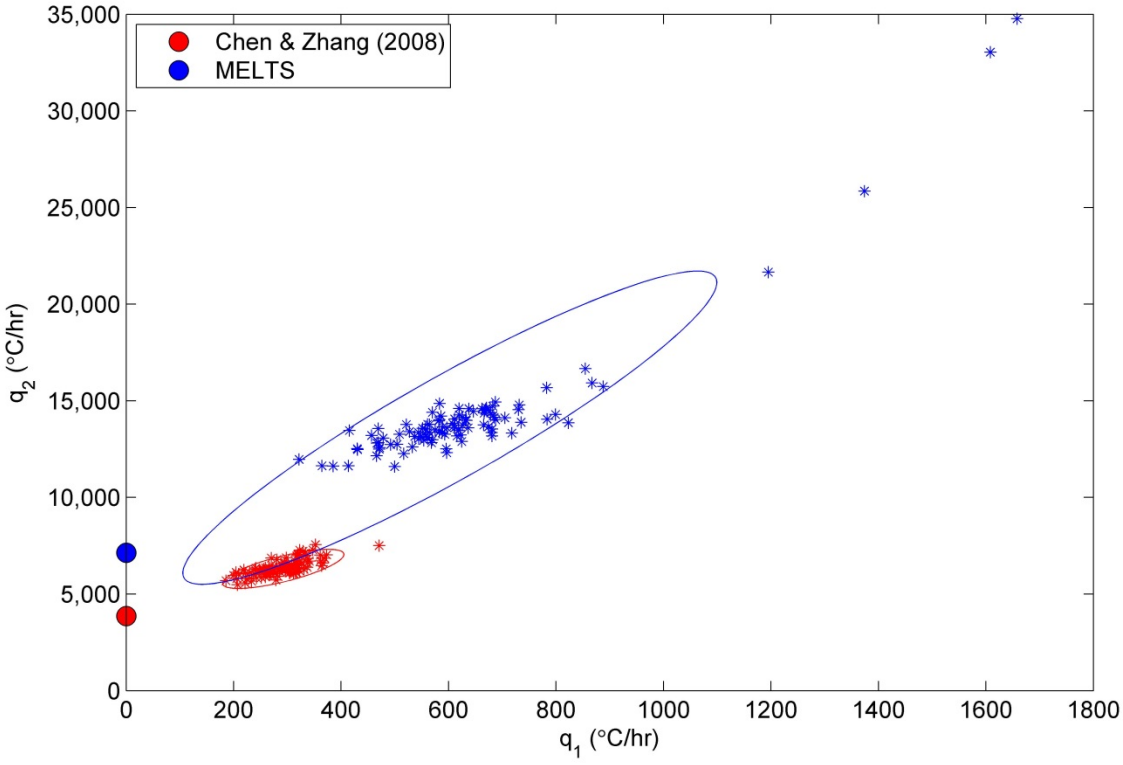

Figure S3 Comparison of best-fit cooling rates for melt inclusion Siq16 using the MgO-temperature relationship of Chen and Zhang (2008) (in red) and MELTS (in blue). Colored circles on the y-axis are results of the single stage cooling model. Small stars indicate the results of fitting MgO data in melt inclusion Siq16 with added noise (from a normal distribution with a standard deviation of 0.1 wt. % MgO). For each of the two thermometers, 100 noisy (synthetic) MgO profiles were fit. Red and blue ellipses are q_1–q_2 95% confidence error ellipses for the best-fit 2-stage cooling histories using the Chen and Zhang (2008) thermometer and MELTS thermometer respectively. The higher temperatures for a given MgO concentration in the liquid that are predicted by MELTS result in a factor of ~2 increase in best-fit cooling rates compared to the Chen and Zhang (2008) model.

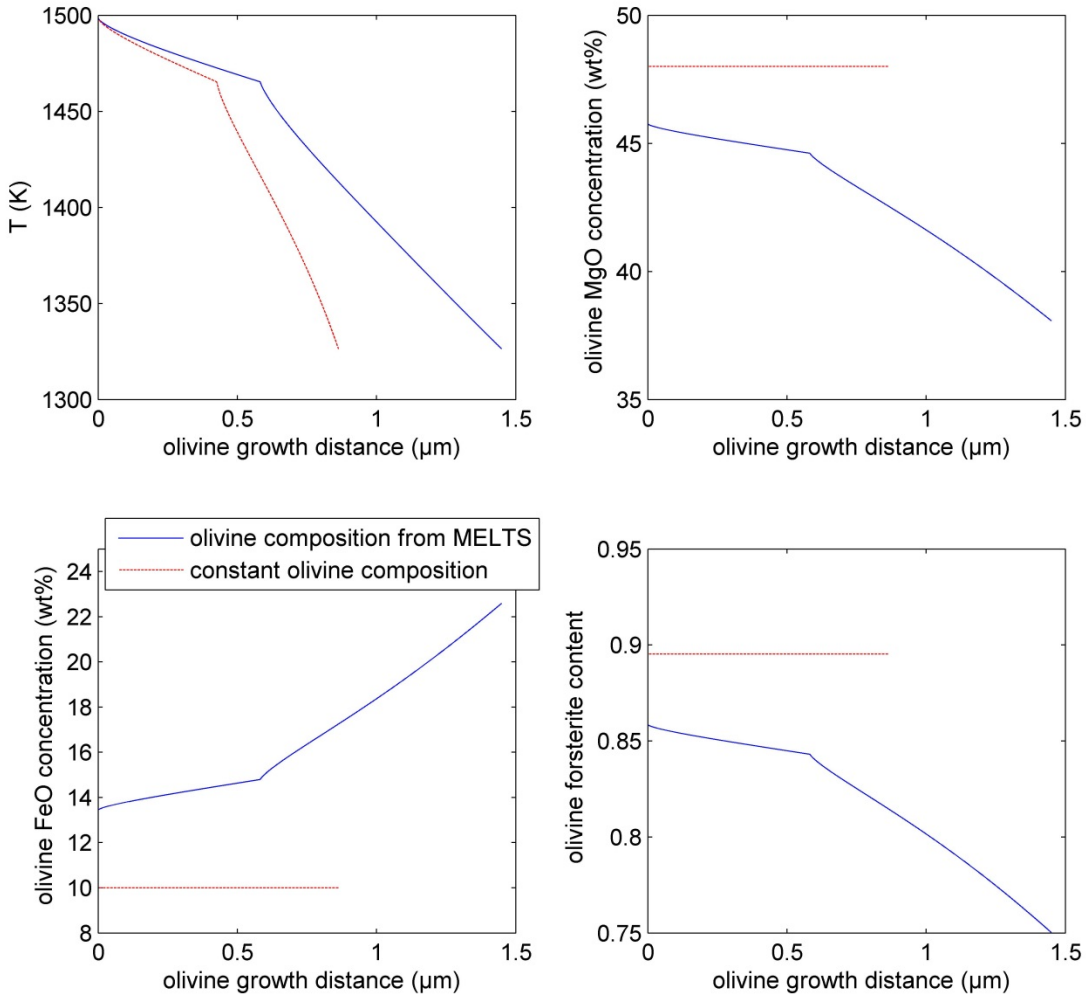

Figure S4 Comparison of the constant olivine composition model (used for the fitting presented in the main text; red lines) with a variable composition olivine model calculated using MELTS (blue lines) for melt inclusion Siq16. The MELTS calculation shown here is the same as the calculation shown in Figures S2 and S3. Using MELTS to calculate the decrease in forsterite content of the olivine as crystallization progresses results in the crystallization of ~50% more olivine than predicted by our constant olivine composition assumption. Although this does not affect the cooling history fitting, it does affect the calculated distribution of Al_2O_3 in the melt inclusions. This effect is explored in Figure S5.

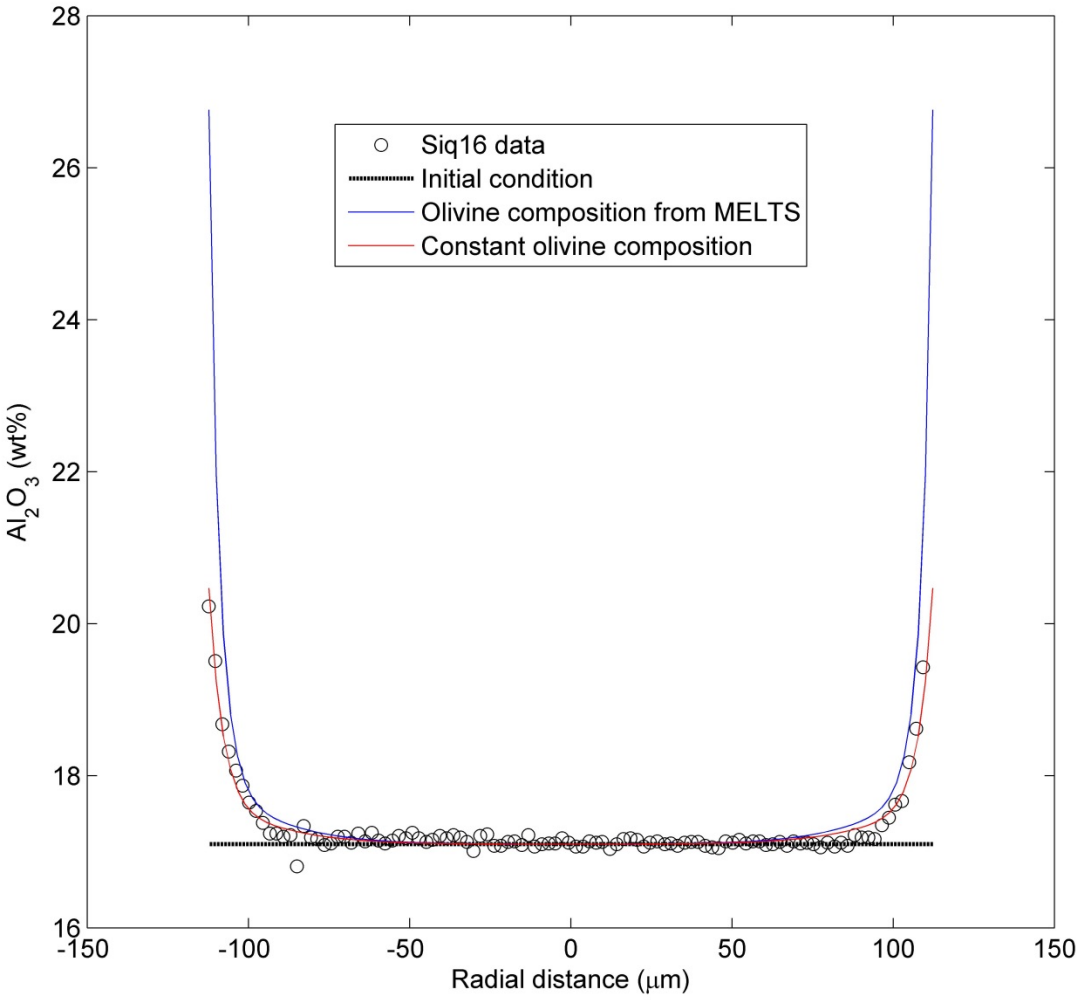

Figure S5 Comparison of the effects of two different models for olivine composition on the fit to Al_2O_3 data from melt inclusion Siq16. Both models follow the best-fit cooling history for Siq16 determined using MELTS (see Figure S2, blue lines). The fit to the Al_2O_3 data is marginally better using a constant composition olivine model. However, it is possible that higher resolution measurements at the olivine-melt interface would reveal a stronger enrichment in Al_2O_3 at the interface than we observed during this study.

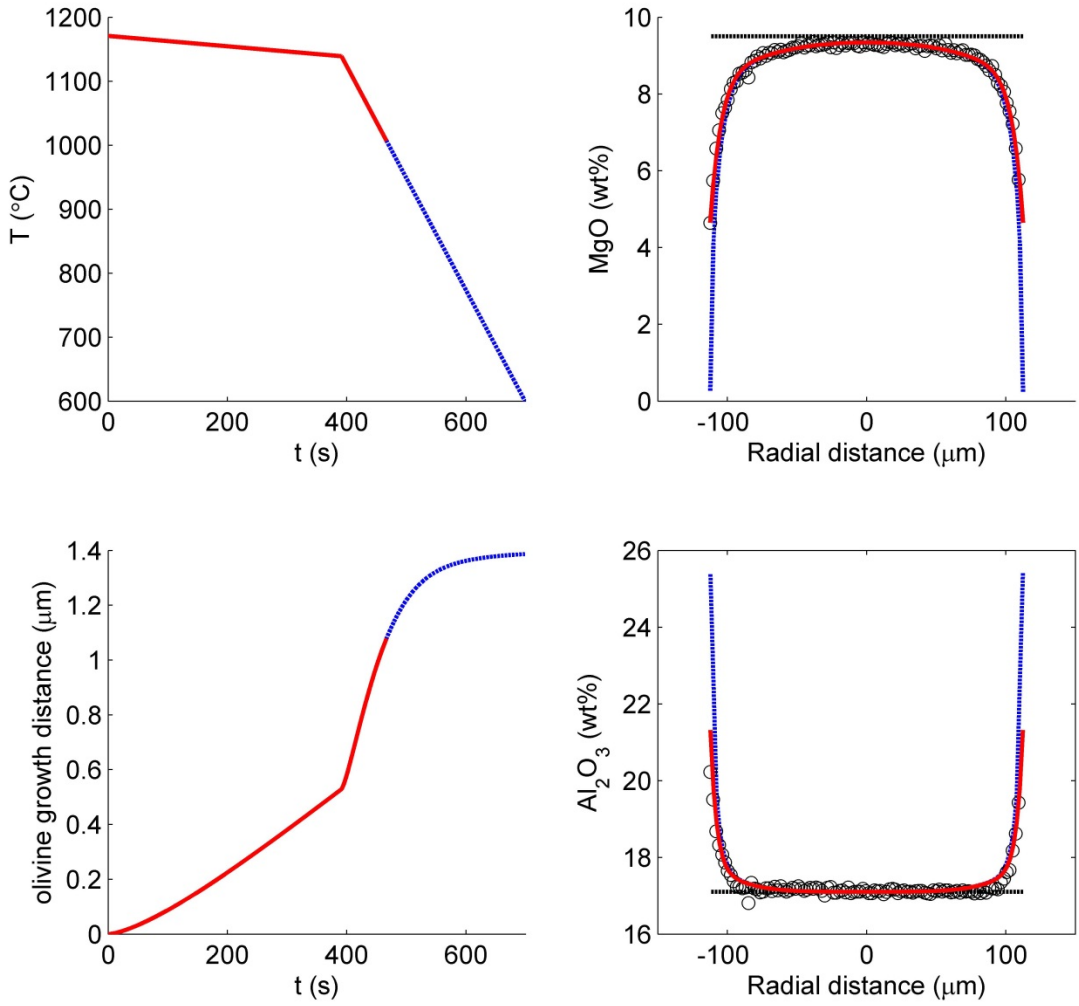

Figure S6 Comparison of two different assumptions for the value of T_{low} (the lowest temperature experienced by the melt inclusion during cooling) for melt inclusion Siq16. The simulation in red fixes T_{low} to be the temperature corresponding to the lowest measured MgO concentration in the melt inclusion (using the thermometer of Chen and Zhang, 2008). This is the assumption applied for the fitting in the main paper, and the curves represent the best-fit cooling history from Table S2. The simulation in blue extends the cooling history (at a fixed cooling rate) to a temperature of 600 °C. This extended cooling history produces ~0.3 μm additional olivine growth. The quality of the match between the model and the MgO and Al_2O_3 data is slightly degraded at the edges of the melt inclusion, although this is a small effect.

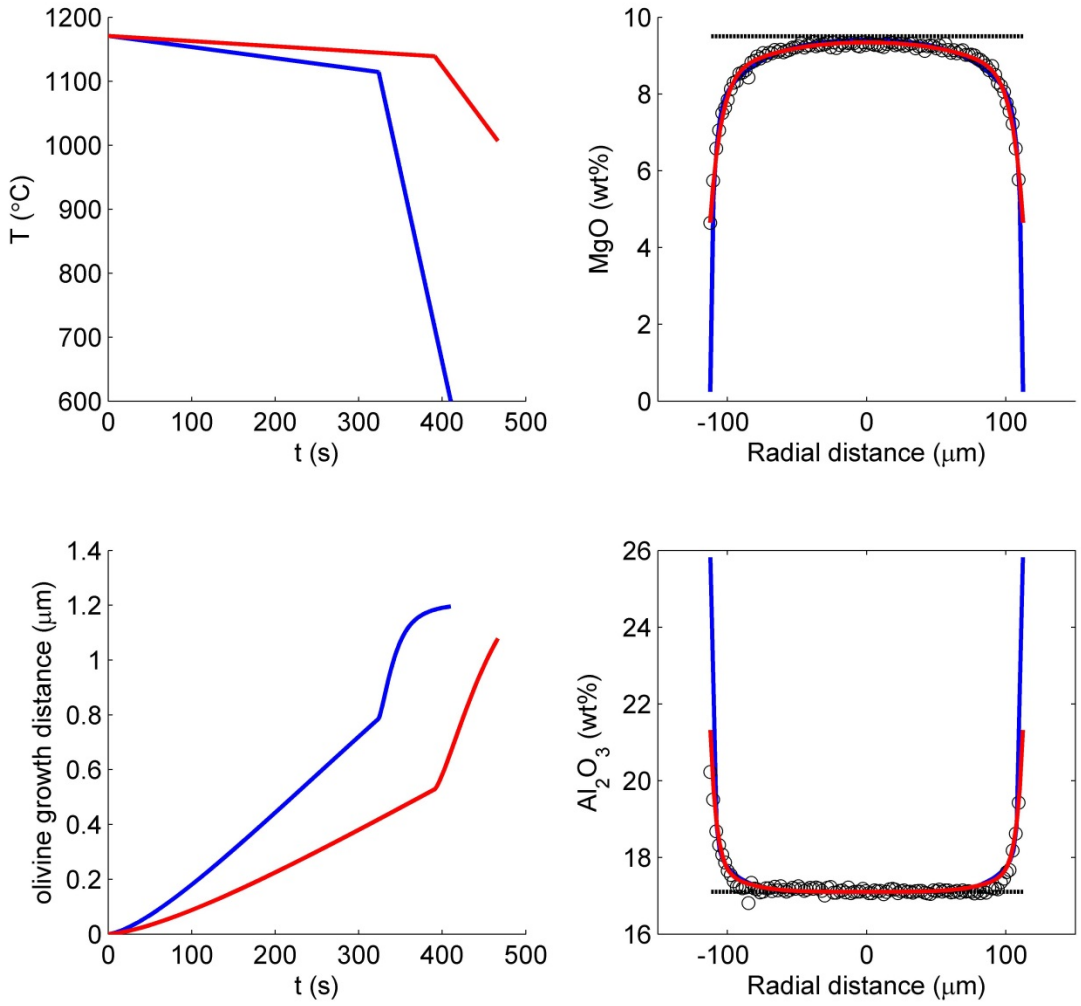

Figure S7 Comparison of two different assumptions for the value of T_{low} (the lowest temperature experienced by the melt inclusion during cooling) for melt inclusion Siq16. The red curves are as on Figure S6 and were calculated by finding the best fit to MgO data in melt inclusion Siq16 fixing T_{low} to the temperature corresponding to the lowest measured MgO concentration in the melt inclusion. The blue curves represent the best fit to the MgO data in Siq16 fixing T_{low} to 600 °C. Although by eye (except at the edges of the melt inclusion) the two models both adequately describe the MgO data, the misfit between the best-fit model and the data is greater when T_{low} is fixed to 600 °C (misfit = 0.2027 for the blue curve, where misfit is defined in the main text—see "The inverse model: using the measured MgO to solve for cooling rate") than it is when T_{low} is fixed to the temperature corresponding to the lowest measured MgO concentration in the melt inclusion (misfit = 0.0060 for the red curve).

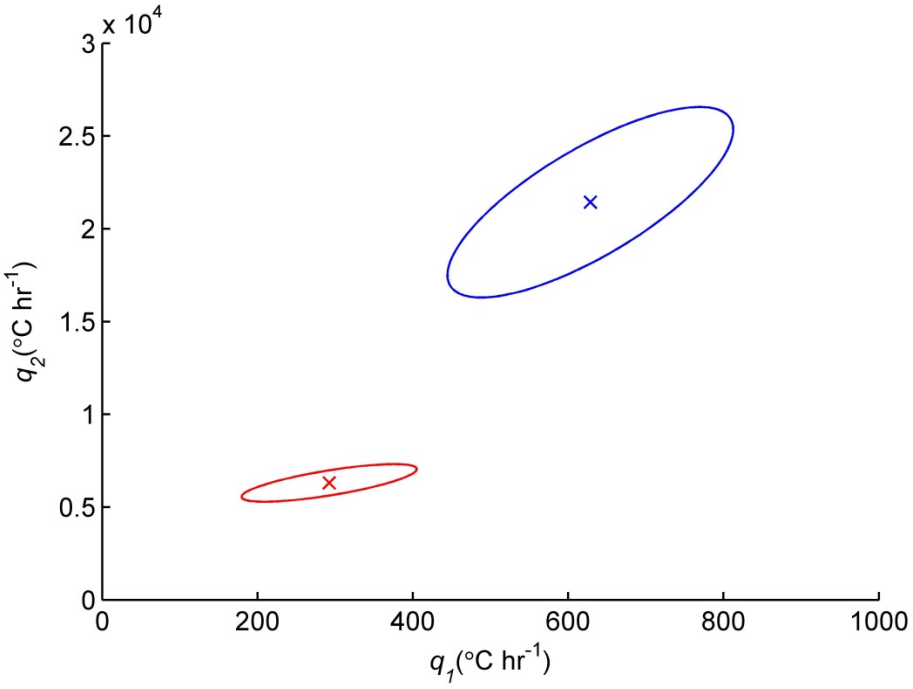

Figure S8 Comparison of q_1-q_2 95% confidence ellipses for melt inclusion Siq16, for different values of T_{low}. The red ellipse is for the case where T_{low} is assumed to be the temperature corresponding to the lowest measured MgO in Siq16 (this is the approach taken in the main paper). The blue ellipse is for the case where T_{low} is fixed to a value of 600 °C. Lowering the value of T_{low} to below the closure temperature for MgO diffusion in the melt inclusion results in an increase in the best-fit cooling rates (by a factor of ~2 for q_1 and a factor of ~3 for q_2). However, this approach slightly degrades the match between the model and the MgO data (see Figure S7). The red cross marks the cooling rates used to create the red curves in Figure S7, and the blue cross marks the cooling rates used to create the blue curves in Figure S7.

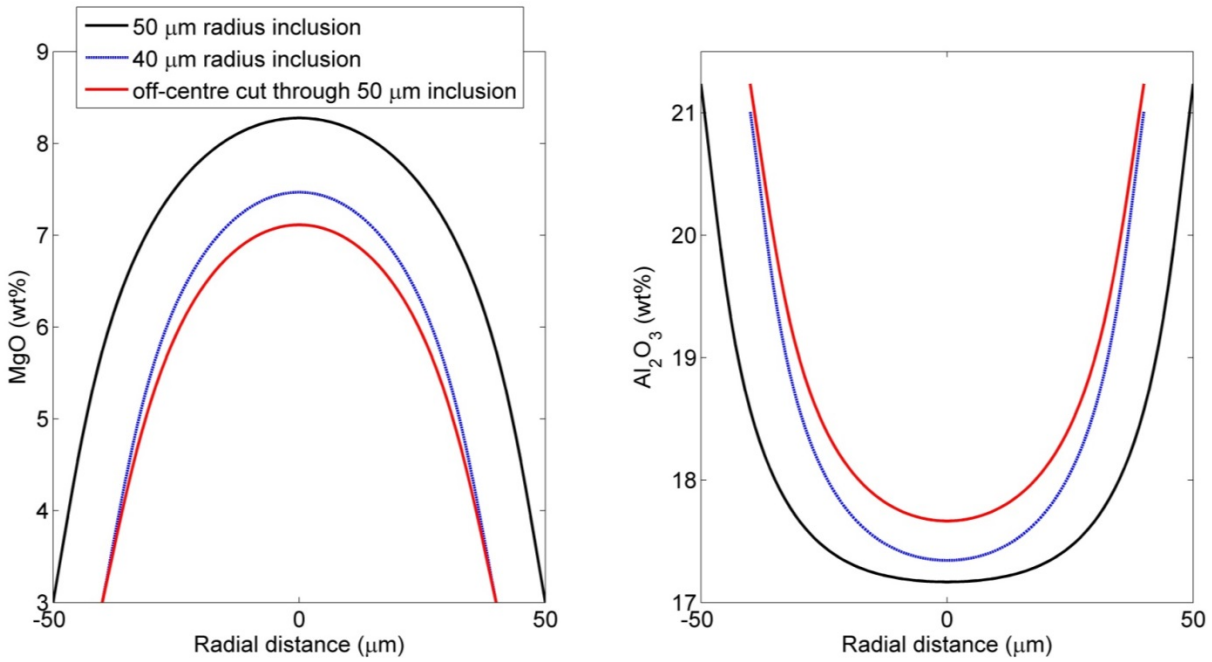

Figure S9 Exploring the effect of an off-center cut through a melt inclusion on its expected MgO and Al_2O_3 concentration profiles. All curves on this figure experienced the same cooling history. The black curves are calculated concentration profiles of MgO and Al_2O_3 for a 50 μm radius inclusion cut through its center. The blue curves are calculated concentration profiles of MgO and Al_2O_3 for a 40 μm radius inclusion cut through its center. The red curves are calculated concentration profiles of MgO and Al_2O_3 for a 50 μm radius inclusion cut along a circular section with a radius of 40 μm. Cutting this melt inclusion along an off-center plane has the effect of lowering its central MgO concentration and raising its central Al_2O_3 concentration. This provides another possible explanation for the discrepancy in initial concentrations of Al_2O_3 required to fit the Al_2O_3 data in pairs of melt inclusions trapped in the same olivine host (see "Testing the two-stage linear cooling model – 2. Modeling zonation of Al_2O_3" in the main text), where we observe that the smaller inclusion in each pair typically requires a higher starting concentration of Al_2O_3.

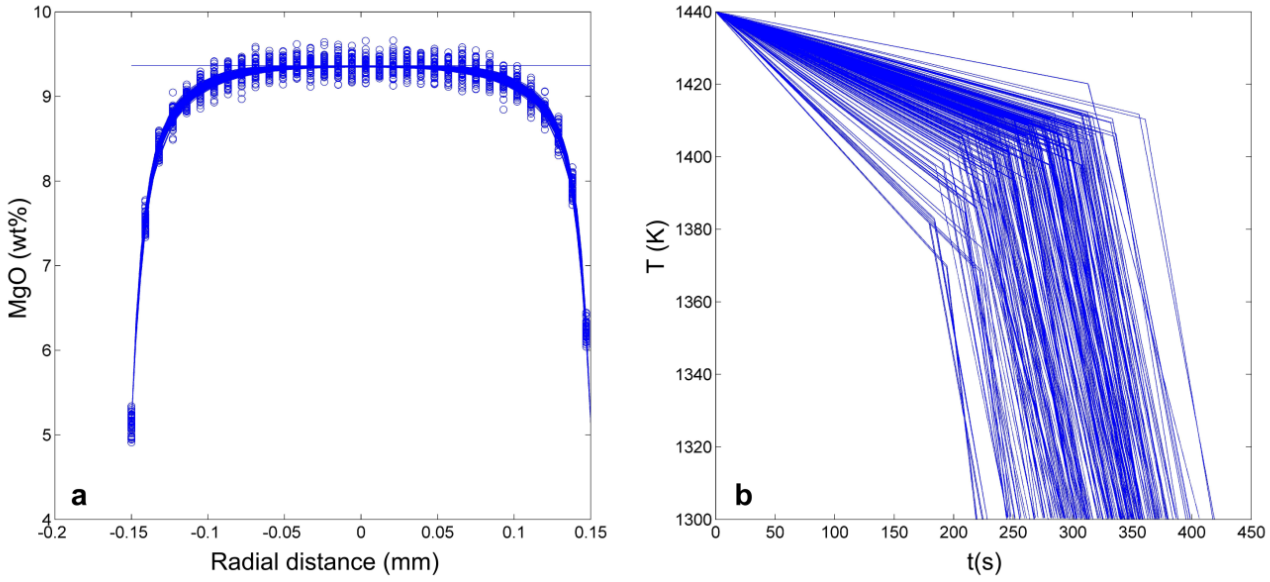

Figure S10 (a) Illustration of the parametric bootstrap inversion technique. 100 noisy MgO concentration profiles across a 150 μm radius melt inclusion are plotted as blue circles. Noisy profiles were created by adding noise (with 1σ=0.1 wt. %) to synthetic data spaced at 10 μm. The best fits to these noisy profiles are plotted as solid blue lines. **(b)** Best-fit two-stage linear cooling histories for the 100 noisy MgO concentration profiles plotted in (a).

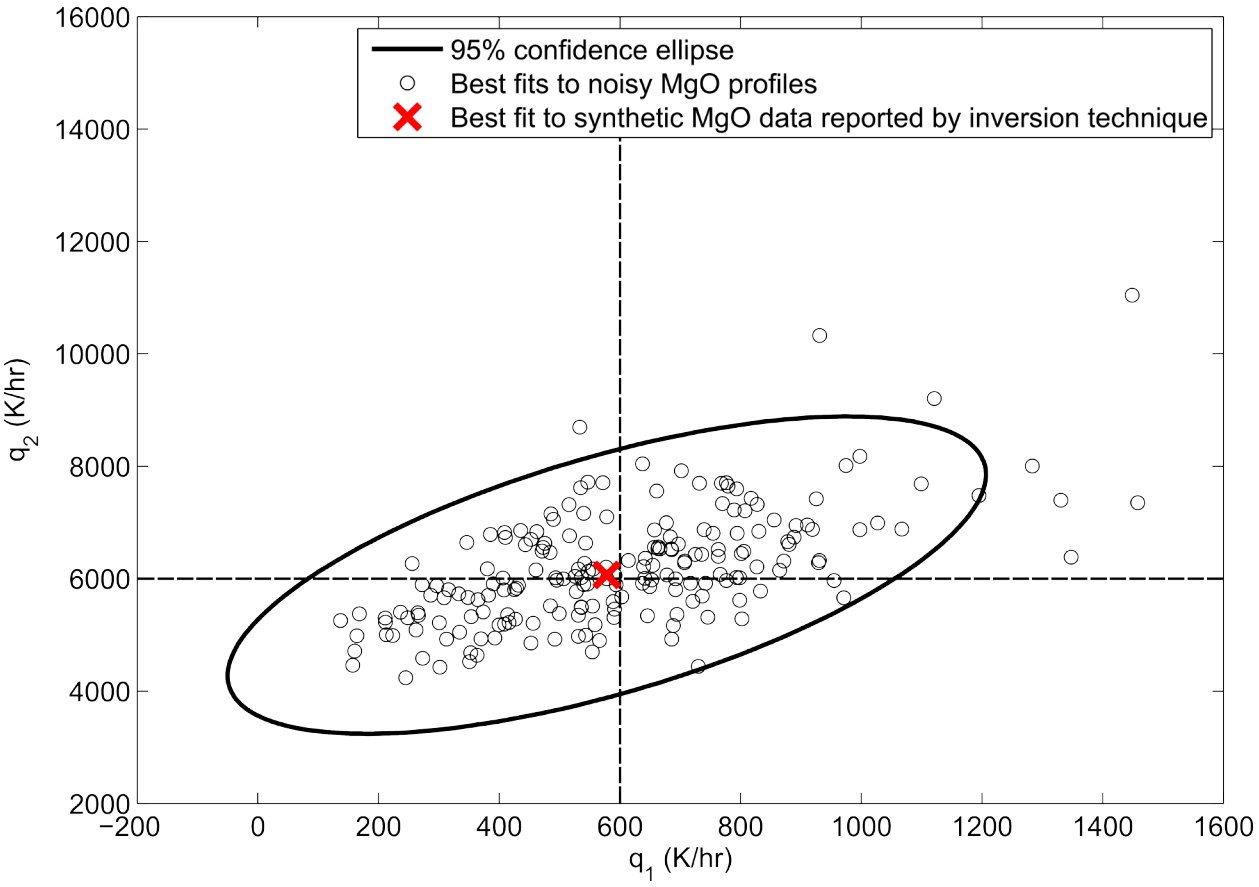

Figure S11 Test of the cooling history inversion technique on a synthetic, 150 μm radius melt inclusion with a known cooling history (T_{mid}=1400 K; q_1=600 K/hr; q_2=6000 K/hr). Best fits to 100 different noisy MgO profiles are plotted as black circles. The 95% confidence ellipse is centered on the median values of q_1 and q_2 (red cross), and these values are output by the inversion technique as the 'overall best-fit' to the original MgO data. The true parameter values are indicated by black dashed lines.

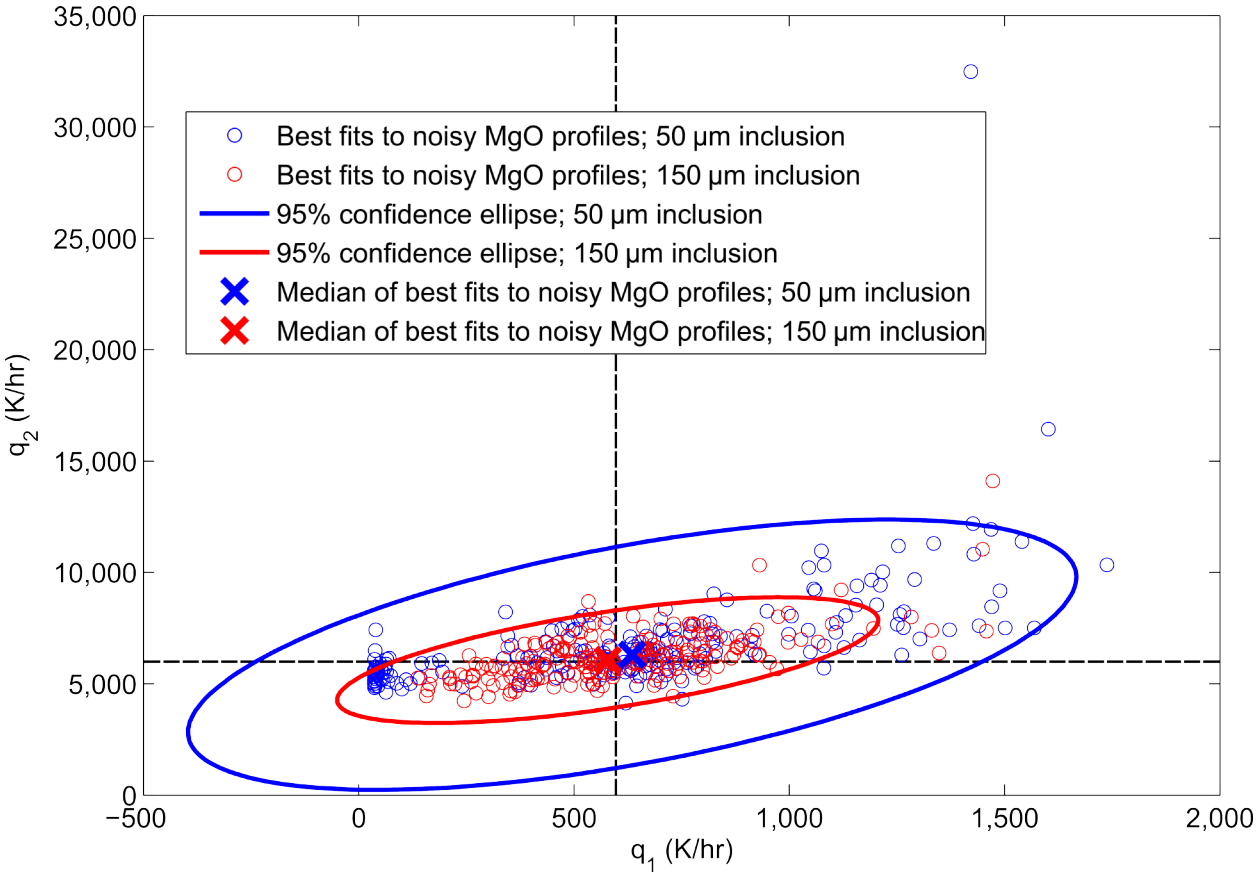

Figure S12 Results of inverting MgO profiles in two modelsynthetic melt inclusions of different sizes with identical, known cooling histories (T_{mid}=1400 K; q_1=600 K/hr; q_2=6000 K/hr – true cooling rates indicated by black dashed lines). The 95% confidence ellipse for the small inclusion (in blue) is larger than the 95% confidence ellipse for the large inclusion (in red), suggesting that cooling history parameters determined from small melt inclusions are less precisely constrained than the parameters determined from large melt inclusions (when MgO measurements are made with the same spatial resolution). However, the accuracy of the technique is not greatly affected in this case: The cooling history parameters for the smaller inclusion are accurate to within 6% and the large inclusion cooling history parameters are accurate to within 4%.

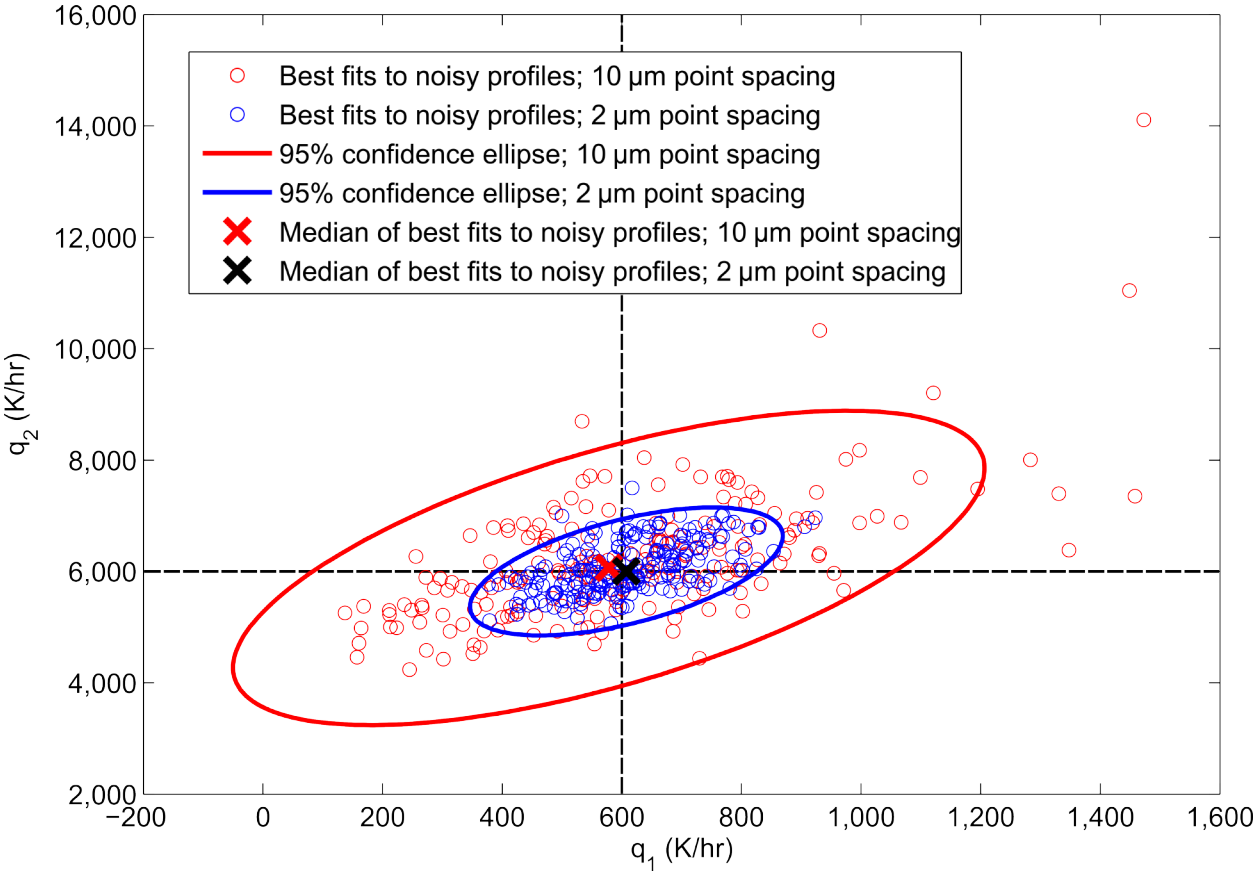

Figure S13 Effect of spatial resolution of MgO concentration measurements on accuracy and precision of inversion technique for synthetic data generated with the following cooling history parameters: T_{high}=1440 K, T_{mid}=1400 K, T_{low}=1300 K, q_1=600 K hr^{-1}, and q_2=6000 K hr^{-1}(true cooling rates indicated by black dashed lines). Increasing the spatial resolution of the MgO profile from 10 to 2 μm point spacing results in an increase in the accuracy of the cooling history parameters (from <4 rel. % to <2 rel. %) and also increases the precision of the inversion technique (as demonstrated by the reduction in the size of the 95% confidence ellipse for the high spatial resolution profile).

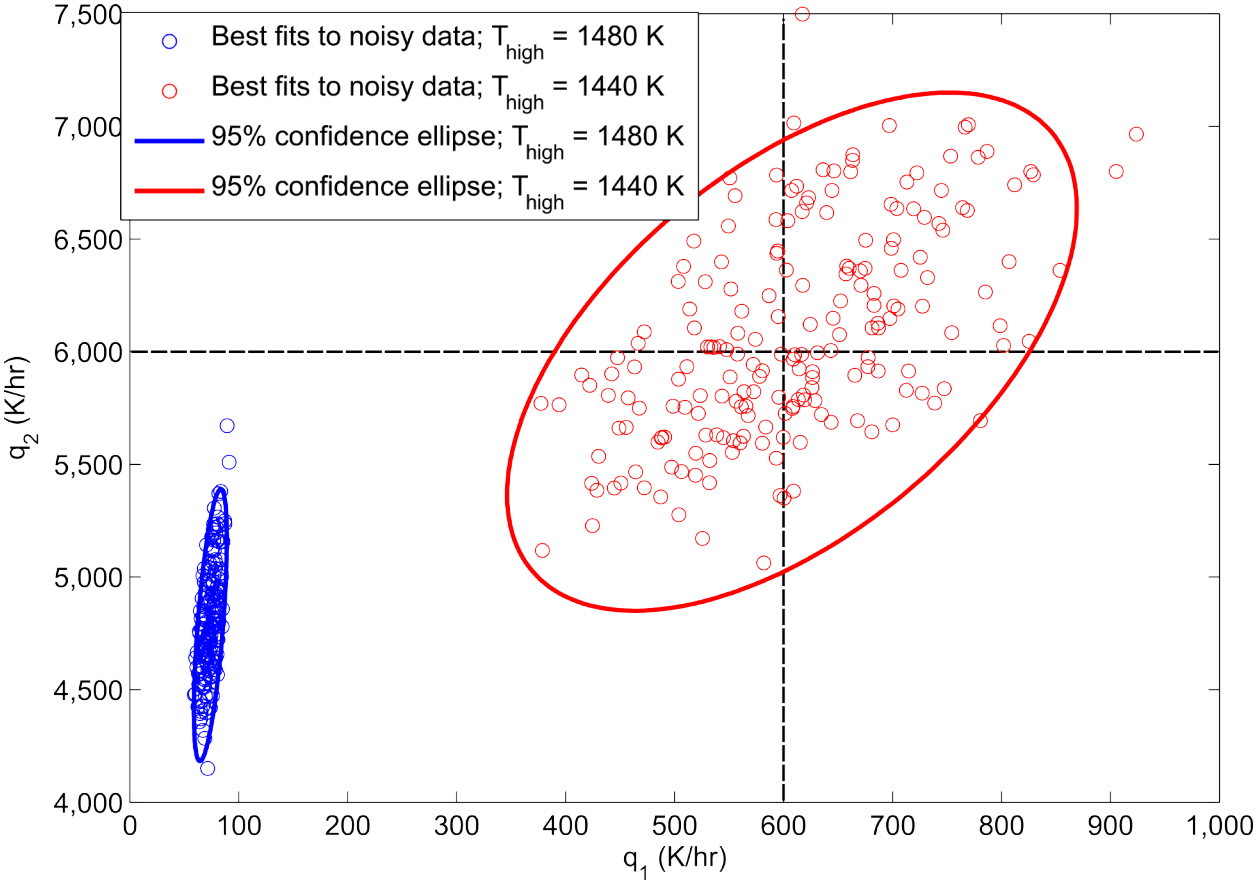

Figure S14 Results of a simulation (with T_{high}=1440 K, T_{mid}=1400 K, T_{low}=1300 K, q_1=600 K hr^{-1}, and q_2=6000 K hr^{-1} – true cooling rates indicated by black dashed lines) to test the effects of overestimating T_{high}. Shown in red are the best fits and the 95% confidence ellipse for an inversion assuming the correct value of T_{high} (i.e., T_{high} = 1440 K). The values of q_1 and q_2 returned by this inversion are within 2 rel. % of their true values. Shown in blue are the best fits and the 95% confidence ellipse for an inversion assuming a value of T_{high} that is 40 K higher than its true value (i.e., T_{high} = 1480 K). Overestimating T_{high} drives q_1 and q_2 to lower values.

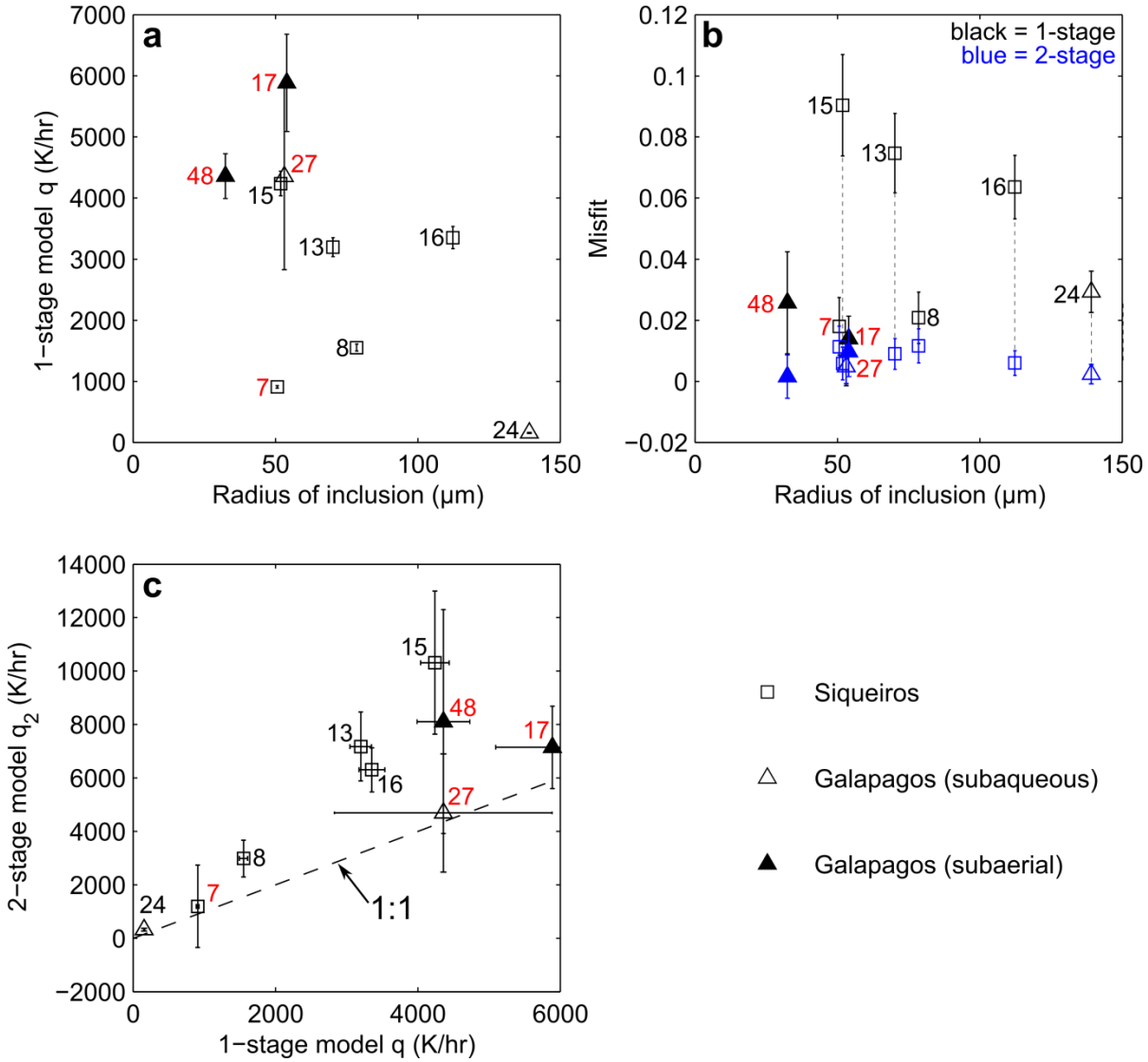

Figure S15 Comparison of best-fit parameters from single-stage and two-stage models for all inclusions with data points spaced 2 μm apart. In each panel, the Siqueiros melt inclusions are plotted as squares and the Galapagos inclusions are plotted as triangles. Each point is labeled with the identification number of the melt inclusion. **(a)** Plot of the cooling rate determined by the single-stage linear cooling model vs. melt-inclusion radius illustrating the negative correlation between cooling rate and inclusion size. Error bars represent ±2σ (where σ is the standard deviation of cooling rates fit to 100 synthetic MgO profiles—see "Inverting the MgO concentration profiles for two-stage cooling histories" in the main text, and Figure S10). **(b)** Plot of the model misfit (see "The inverse model: using the measured MgO to solve for cooling rate" in the main text for definition of misfit) vs. the melt inclusion radius for fits to both the single-stage linear cooling model (in black) and the two-stage linear cooling model (in blue). Single-stage linear cooling model fits are labeled with the identification number of the melt inclusion and are joined to the two-stage model fits of the same melt inclusion by a thin dashed black line. Error bars represent ±2σ (standard deviation) of the misfits determined by fitting 100 synthetic MgO profiles. **(c)** Relationship between best-fit values of q_2 (the second constant cooling rate in the two-stage linear cooling model) and best-fit values of q (the cooling rate in the single-stage linear cooling model). A 1:1 line is plotted for reference (black dashed line). Melt inclusions for which q and q_2 overlap at 2σ are labeled in red. These inclusions are described well by the single-stage cooling model and the improvement by going to the two-stage model is small. Note that in (b), the misfit of the single-stage cooling model is relatively low for these inclusions. For those melt inclusions whose identification number is written in black, q and q_2 do not overlap at 2σ. These melt inclusions are poorly fit by the single-stage model (they have high misfit values in (b) and the single-stage model underestimates their final cooling rate.

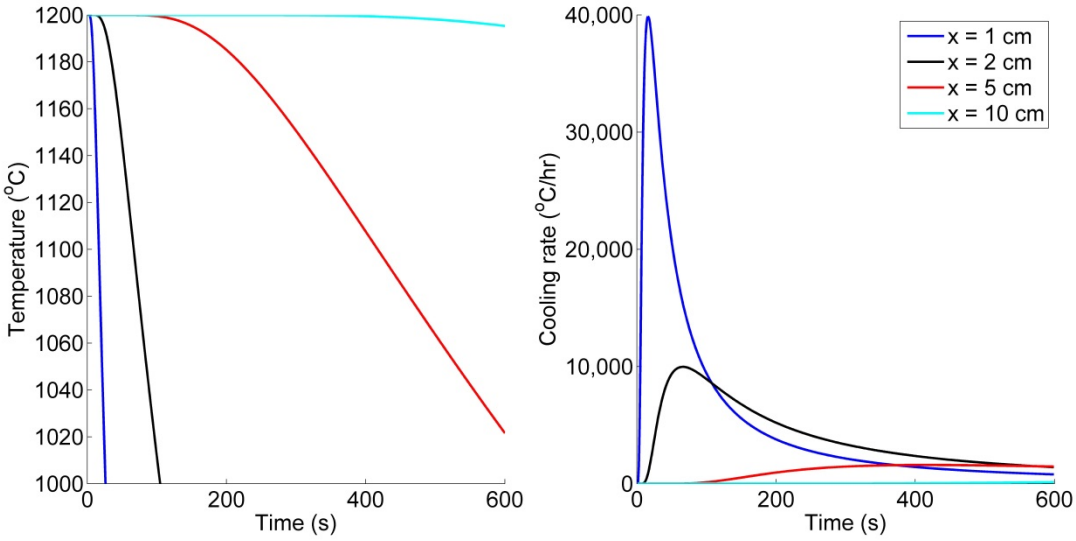

Figure S16 Thermal histories during cooling from 1200 °C to 2 °C calculated using an analytical solution for conductive cooling in a semi-infinite medium with a constant temperature boundary condition (i.e., the lava-water interface is held at 2 °C) (Crank 1975). The best-fit values of q_2 recorded by the melt inclusions (see Table S2) are consistent with conductive cooling at distances of a few centimeters from the lava-water or lava-air interface.

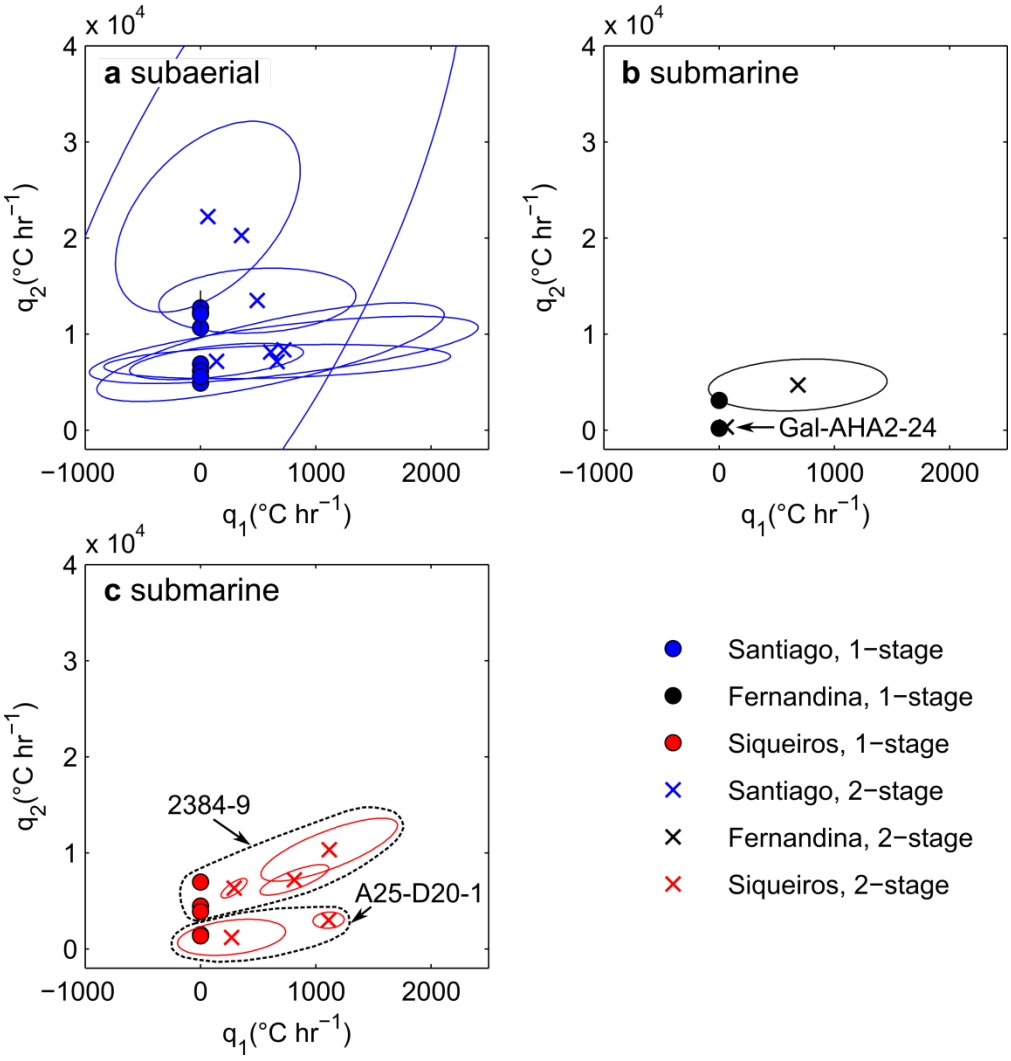

Figure S17 q_1-q_2 95% confidence error ellipses for all of the melt inclusions that were measured with 2μm point spacing. Compare with Figure 10 in the main paper, for which 95% confidence ellipses were calculated for $\log_{10}(q_1)$-$\log_{10}(q_2)$. The median values of q_1 and q_2 are marked by crosses. The colored circles plotted along q_1=0 are the results of the single-stage linear cooling model. The best fit cooling rates determined by the single-stage linear cooling model tend to be similar to but systematically low relative to the best-fit values for q_2 (colored squares), and the relative order of best-fit cooling rates is successfully predicted by the single-stage model. **(a)** Subaerially quenched Santiago melt inclusions. These inclusions tend to be well-described by single-stage cooling histories (e.g., Gal-STG-17 on Fig. 9), so their q_1-q_2 error ellipses for the 2-stage cooling model are relatively poorly constrained, with some best fit cooling rates extending to arbitrarily high values. This asymmetry in the distribution of best fit cooling histories causes the 95% confidence ellipses to extend to unphysical negative cooling rates. As presented in the main paper, best fit values of q_1 and q_2 for these inclusions are better described by a lognormal distribution. (**b)** Submarine Fernandina melt inclusions. Symbols as in (a). Note that the cooling history for Gal-AHA2-24 is so well-constrained that its error ellipse is barely visible at this scale. **(c)** Siqueiros melt inclusions. All samples in this panel are from one of two locations (see Table S1): Siq7 and Siq8 are from dredge A25-D20-1; Siq13, Siq15 and Siq16 were collected during an Alvin submersible dive, and the thermal histories of melt inclusions from these different locations group together.